




Λ polarization in very high energy heavy ion collisions as a probe of the quark–gluon plasma formation and properties

Andrea Palermo^{1,a} , Eduardo Grossi², Iurii Karpenko³, Francesco Becattini²

¹ Department of Physics and Astronomy, Center for Nuclear Theory, Stony Brook University, Stony Brook, NY 11794-3800, USA

² Università di Firenze and INFN Sezione di Firenze, Via G. Sansone 1, 50019 Sesto Fiorentino, Florence, Italy

³ Faculty of Nuclear Sciences and Physical Engineering, Czech Technical University in Prague, Břehová 7, 11519 Prague 1, Czech Republic

Received: 29 April 2024 / Accepted: 10 August 2024
© The Author(s) 2024

Abstract We have studied the spin polarization of Λ hyperons in heavy ion collisions at center-of-mass energies $\sqrt{s_{NN}} = 200$ GeV and $\sqrt{s_{NN}} = 5.02$ TeV carried out at RHIC and LHC colliders. We have calculated the mean spin vector at local thermodynamic equilibrium, including all known first-order terms in the gradients of the thermo-hydrodynamic fields, assuming that the hadronization hypersurface has a uniform temperature. We have also included the feed-down contributions to the polarization of Λ stemming from the decays of polarized Σ^* and Σ^0 hyperons. The obtained results are in good agreement with the data. In general, the component of the spin vector along the global angular momentum, orthogonal to the reaction plane, shows strong sensitivity to the initial longitudinal flow velocity. Furthermore, the longitudinal component of the spin vector turns out to be very sensitive to the bulk viscosity of the plasma at the highest LHC energy. Therefore, the azimuthal dependence of spin polarization can effectively constrain the initial hydrodynamic conditions and the transport coefficients of the quark gluon plasma.

1 Introduction

After its measurement by STAR collaboration in 2017 [1], spin polarization has become an important probe in relativistic heavy ion collisions (for reviews, see [2–4]). From a theoretical standpoint, the most successful approach is the hydrodynamic-statistical model where spin polarization is calculated at local thermodynamic equilibrium at hadronization when the quark gluon plasma (QGP) gives rise to hadronic particles which rapidly decouple and freely stream to the detectors.

^a e-mail: andrea.palermo@stonybrook.edu (corresponding author)

In the local equilibrium model, the sources of the spin polarization vector of fermions are the gradients of the hydro-thermodynamic fields, that is, temperature, velocity, and chemical potential. Even if, for some time, spin polarization was mostly connected to vorticity (more precisely, thermal vorticity [5–8]), it has become recently clear that also the symmetric gradient of the four-temperature (thermal shear tensor) and the gradient of the chemical potential [9–11] are responsible for a large contribution to local polarization, even though the global polarization is essentially determined by the thermal vorticity [12].

Particularly in very high energy collisions where the chemical potentials are negligible and the hadronization hypersurface Σ can be approximated by an isothermal one, the mean spin polarization vector of Dirac fermions such as the Λ hyperons with momentum p is given by [13]¹:

$$S^\mu(p) = -\epsilon^{\mu\rho\sigma\tau} p_\tau \frac{\int_\Sigma d\Sigma \cdot p n_F (1 - n_F) \left[\omega_{\rho\sigma} + 2 \hat{t}_\rho \frac{p^\lambda}{\varepsilon} \Xi_{\lambda\sigma} \right]}{8mT_H \int_\Sigma d\Sigma \cdot p n_F}, \quad (1)$$

¹ It is important to point out that the formula (1) somewhat differs from others that have been used in other numerical studies [14–18], for a twofold reason. First, the Eq. (1) is appropriate for an isothermal hadronization hypersurface and not for a general one hence it is specifically applicable to very high energy, where it is a better approximation than the general formula, including temperature gradients (see discussion in [13]). Second, the energy $\varepsilon = p \cdot \hat{t} = p^0$ is, in some studies, replaced by $p \cdot u$ where u is the four-velocity field; this change leads to significant quantitative differences. Indeed, in Ref. [12] the authors reproduce the correct sign of $P_z(\phi)$ without the isothermal decoupling but using $p \cdot u$, and this would not have been the case had they used p^0 [19]. We stress that the derivation adopted in Ref. [9] requires to use p^0 .

where T_H is the hadronization temperature, $\hat{t}^\mu = \delta_0^\mu$ is the time unit vector in the QGP centre-of-mass frame, $\varepsilon = p \cdot \hat{t}$ and $n_F = [e^{\beta \cdot p - \sum_i \mu_i/T} + 1]^{-1}$ is the Fermi distribution (the chemical potentials can be taken as vanishing at the considered energies). The presence of a specific time vector is a manifestation of the dependence of the above formula on the specific hadronization hypersurface, which in turn is related to the non-conservation of the local equilibrium operator (see discussion in Ref. [9]). The tensors $\omega_{\mu\nu}$ and $\Xi_{\mu\nu}$ are the kinematic vorticity and shear, respectively:

$$\begin{aligned}\omega_{\mu\nu} &= \frac{1}{2} (\partial_\nu u_\mu - \partial_\mu u_\nu), \\ \Xi_{\mu\nu} &= \frac{1}{2} (\partial_\nu u_\mu + \partial_\mu u_\nu).\end{aligned}\quad (2)$$

The formulae (1) and (2) make it apparent that, unlike most other hadronic observables, spin polarization is sensitive to the flow velocity gradients at leading order. Therefore, polarization can be used as an important observable to constrain various medium parameters, as we will show in the present study.

Over the past few years, there have been several Λ polarization numerical studies with the hydrodynamic model of the QGP based on thermal vorticity [20–25] or including also the shear tensor contribution [12–18, 26–28]. In this paper, we have carried out full numerical simulations of Au–Au at $\sqrt{s_{NN}} = 200$ GeV and Pb–Pb collisions at $\sqrt{s_{NN}} = 5020$ GeV and compared the obtained results to the available experimental data, employing up-to-date theoretical formulae for spin polarization. Furthermore, we have studied the sensitivity of spin polarization to the initial conditions and transport coefficients, specifically the shear and bulk viscosity. For the first time, we have included in a realistic hydrodynamic simulations the corrections due to the decay of polarized Σ^* and Σ^0 (the so-called feed-down corrections) to the local polarization. Additionally, we have studied the impact of varying the initial longitudinal momentum flow in the initial state, showing that the local polarization along the total angular momentum is quite sensitive to it. It should be pointed out that such a dependence was studied in great detail in Ref. [17], for Au–Au collisions at $\sqrt{s_{NN}} = 27$ GeV. In order to avoid possible biases, we have employed two initial state models.

The paper is organized as follows. In Sect. 2 we describe and validate the hydrodynamic simulation setup using two different initial state models. Section 3 is devoted to the study of feed-down corrections to the polarization vector, and in Sect. 4, we calculate various polarization observables measured experimentally. Finally, we address the effect of the initial collective flow and viscosity on polarization in Sect. 5.

Notation

We adopt the natural units in this work, with $\hbar = c = K = 1$. The Minkowskian metric tensor g is $\text{diag}(1, -1, -1, -1)$; for the Levi-Civita symbol we use the convention $\epsilon^{0123} = 1$. We will use the relativistic notation with repeated indices assumed to be summed over.

2 Numerical framework

The numerical setup used in this work builds upon the chain of codes `vHLLC` and `SMASH` [29–32]. Such a chain involves a pre-defined initial state, a 3+1D viscous hydrodynamic evolution of the produced dense medium, a fluid-to-particle transition (hadronization, or, more technically *particlization*), taking place at a surface of fixed energy density, followed by a Monte-Carlo hadronic sampling from the particlization hypersurface and a subsequent hadronic rescattering and resonance decays.

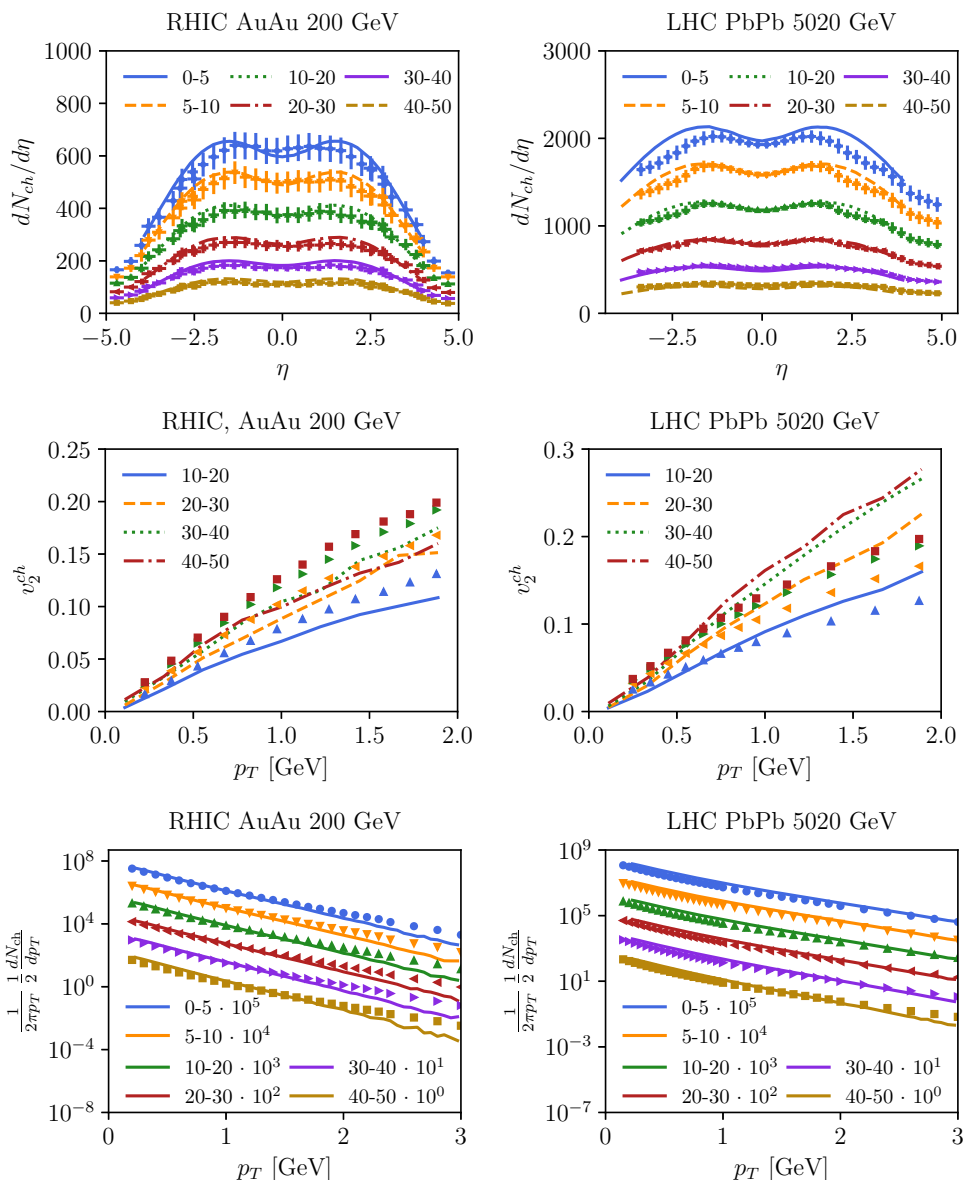
The hydrodynamic evolution is simulated with `vHLLC` code [29], where the particlization hypersurface is reconstructed with `Cornelius` subroutine [33]. This hypersurface is identified as the constant-energy-density hypersurface $e = 0.4$ GeV/fm³, and it is used both for the evaluation of Λ polarization as well as for conventional Monte-Carlo sampling of hadrons using `smash-hadron-sampler` code [34]. Finally, `SMASH` [32] handles rescatterings of the produced hadrons and decays of unstable resonances. We emphasize that spin degrees of freedom are not implemented in `SMASH` therefore, all the polarization results presented in this work (and so far in the literature) are solely based on formula (1) and the subsequent calculation of polarization transfer in the decay of resonances. The polarization calculations are performed using a dedicated code, `hydro-foil`, which is publicly available [35]. To conveniently handle all the chain stages, we have created a hybrid model based on the Python programming language and `Snakemake` [36,37].

As has been mentioned, we have used two Initial State (IS) models in this study. The first one is `superMC`, numerically implemented from scratch based on the formulae from [12,38]. `superMC` is based on Glauber geometry with local energy and momentum conservation conditions and provides a $\sqrt{T_A T_B}$ scaling of the energy density similar to `TrENTo` [46] $p = 0$ initial state. The second is a 3D extension of the initial state from Monte Carlo Glauber generator `GLISSANDO` [47], where entropy depositions from participant nucleons are taken to be tilted in space-time rapidity according to [48], whereas the depositions from binary scatterings are symmetric in space-time rapidity. With either IS option, we have used the starting time of the fluid stage τ_0 and shear viscosity to entropy density ratio η/s values that are considered optimal to reproduce basic hadronic observables.

Table 1 Values of the free parameters in the initialization of the hydrodynamic stage using *superMC*. For a detailed description of these initial condition parameters, see Refs. [12,38]

Parameter	Description	@RHIC AuAu 200 GeV	@LHC PbPb 5020 GeV
w [fm]	Size of the initial hot spot	0.8	0.14
η_0	Size of the mid-rapidity plateau	2.2	2.7
σ_η	Space-time rapidity fall off width	0.9	1.2
f	Initial longitudinal flow fraction	0.15	0.15

Fig. 1 Comparison between model and data with *superMC* initial conditions. Left panels correspond to Au–Au collisions at $\sqrt{s_{NN}} = 200$ GeV at RHIC and the right ones to $\sqrt{s_{NN}} = 5020$ GeV Pb–Pb collisions at LHC. In the upper panels, we show the pseudo-rapidity distribution of charged hadrons, with data from [40] and [41], the mid-panels show the elliptic flow of charged hadrons, data from Refs. [42] and [43], and the lower panels show the transverse momentum spectrum of charged hadrons, with data from Refs. [44] and [45]



In the case of *superMC* IS, the starting time of the fluid stage is $\tau_0 = 1$ fm/c and, unless otherwise stated, a fixed shear viscosity over entropy density ratio of $\eta/s = 0.08$. In the case of 3D *GLISSANDO* IS, the initial time is $\tau_0 = 0.4$ fm/c, $\eta/s = 0.08$ at RHIC energy and $\eta/s = 0.1$ at LHC energy, which reflects a somewhat higher temperature range probed in heavy-ion collisions at the LHC. Instead, for the

bulk viscosity over entropy density ζ/s , we have used the temperature-dependent parametrization introduced in [49], referred to as parametrization III in Sect. 5 (see Eq. 12).

For $\sqrt{s_{NN}} = 200$ GeV energy, the values of the free parameters of the *superMC* IS model have been slightly modified with respect to those originally published in [12,38] to obtain an optimal description of the pseudo-rapidity dis-

Table 2 Values of the free parameters in the initialization of hydrodynamic stage using 3D Glissando IS. For a detailed description of these initial condition parameters, see Ref. [39]

Parameter	Description	@RHIC AuAu 200 GeV	@LHC PbPb 5020 GeV
R [fm]	Size of the initial hot spot	0.4	0.4
η_0	Size of the mid-rapidity plateau	1.5	2.4
σ_η	Space-time rapidity fall off width	1.4	1.4
η_M	Initial state tilt parameter	2.0	4.5
α	Fraction of binary scatterings	0.15	0.15

tribution, elliptic flow of charged hadrons, and transverse momentum spectrum of identified hadrons. For $\sqrt{s_{NN}} = 5020$ GeV, a different optimal tuning has been found, with the values for both energies reported in Table 1. We have used an average initial state of 20k `superMC` events for the tuning. Figure 1 shows the results of our calculations compared to the experimental data. Baryon and electric charge currents do not play a significant role in collisions at the energies under consideration, so the free parameters associated with them, η_{B0} , σ_{Bin} and σ_{Bout} , are the same as the ones reported in Ref. [38] for Au–Au collisions at $\sqrt{s_{NN}} = 200$ GeV.

The 3D extension of `GLISSANDO` initial state is taken from the study in Ref. [39], and it follows a parametrization previously reported in [50]. Differently from Ref. [39], we have not computed the normalization of the initial state energy density by identifying the total energy of the fluid with the sum of energies of incoming participants. Instead, we have treated normalization as another free parameter and tuned it to fit charged hadron $dN/d\eta$ distribution. The resulting parameters are reported in Table 2, and Fig. 2 shows the results of our calculations. We generally have a very good agreement of transverse momentum spectra and pseudo-rapidity distributions of charged hadrons at various centralities but a less good agreement for their elliptic flow coefficient. We attribute the underestimated elliptic flow signal with both initial states to fluid dynamic description with averaged initial state, as compared to event-by-event fluid-dynamic picture in other studies. We also note that at the LHC energy the agreement with the data is better, as the ensuing fluid stage has a longer lifetime, therefore the final flow is somewhat less sensitive to the presence of fluctuations in the initial stage.

3 Feed-down contribution to polarization

The hydrodynamic-statistical model predicts that all particles created by the particlization of the QGP are polarized. When unstable particles are produced in this stage, they transfer part of their polarization to their decay products. Therefore, secondary Λ s produced by decaying heavier particles or resonances are also polarized. The contribution to

polarization owing to the secondary Λ s is called feed-down correction. As the experiments can subtract Λ s from long-lived weakly decaying hadrons, we only consider short-lived hadrons decaying through electromagnetic or strong interaction. Specifically we focus on $\Sigma^* \rightarrow \Lambda + \pi$ and $\Sigma^0 \rightarrow \Lambda + \gamma$, which provide the predominant channels to secondary Λ production.

The polarization transferred from a particle to its decay products in a two-body decay, has been extensively studied elsewhere [51–53]; herein, we briefly review it and describe the formulae used to compute it. Let us then consider the general decay $M \rightarrow \Lambda D$. The particle M produced at hadronization is polarized, and, if it is a fermion, its mean spin vector can be obtained by simply rescaling the Eq. (1) [51–54]:

$$S^\mu(p) = -\frac{S(S+1)}{3} \epsilon^{\mu\rho\sigma\tau} p_\tau \frac{\int_\Sigma d\Sigma \cdot p n_F (1 - n_F) \left[\omega_{\rho\sigma} + 2 \hat{t}_\rho \frac{p^\lambda}{\epsilon} \Xi_{\lambda\sigma} \right]}{2mT_H \int_\Sigma d\Sigma \cdot p n_F}, \quad (3)$$

where S is the spin of the fermion. As it has been discussed, the produced Λ is polarized. The spin vector $\mathbf{S}_*^{(M)}$ of the Λ particle in its rest frame² inherited from the mother particle is [53]:

$$\mathbf{S}_*^{(M)}(\mathbf{p}) = \frac{\int d\Omega_* n(\mathbf{P}) F(\mathbf{p}, \Omega_*) \mathbf{S}_{M \rightarrow \Lambda}(\mathbf{P}, \mathbf{p})}{\int d\Omega_* n(\mathbf{P}) F(\mathbf{p}, \Omega_*)}. \quad (4)$$

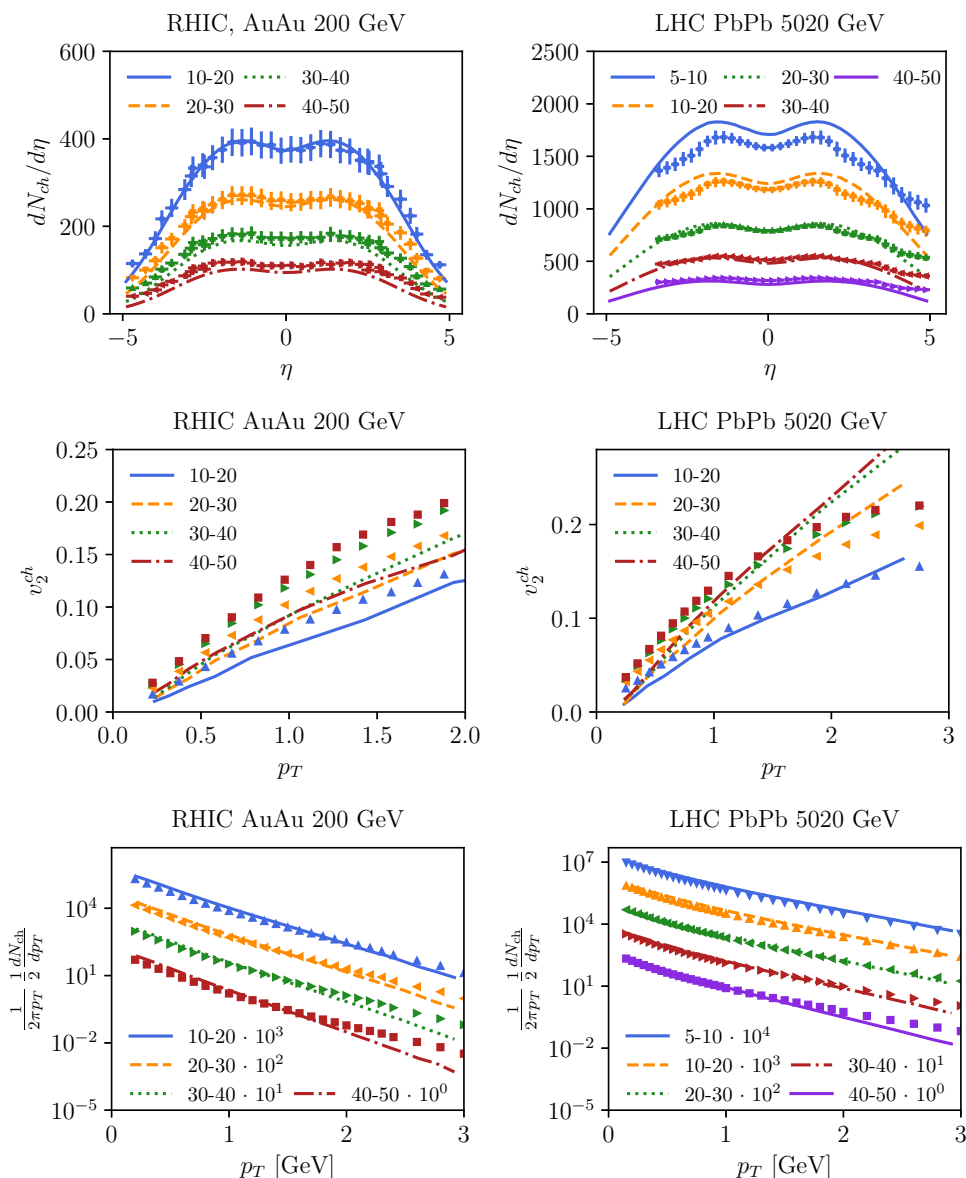
In the above formula, the solid angle Ω_* is in the rest frame of the mother particle, \mathbf{p} and \mathbf{P} are the momenta of Λ and M respectively in the QGP frame and $\mathbf{S}_{M \rightarrow \Lambda}$ is a “spin-transfer” vector function depending on the decay. For the aforementioned decays, they read:

$$\mathbf{S}_{\Sigma^* \rightarrow \Lambda}(\mathbf{P}, \mathbf{p}) = \frac{2}{5} \left(\mathbf{S}_{*\Sigma^*}(\mathbf{P}) - \frac{1}{2} \hat{\mathbf{p}} \cdot \mathbf{S}_{*\Sigma^*}(\mathbf{P}) \hat{\mathbf{p}} \right) \quad (5a)$$

$$\mathbf{S}_{\Sigma^0 \rightarrow \Lambda}(\mathbf{P}, \mathbf{p}) = -\hat{\mathbf{p}} \cdot \mathbf{S}_{*\Sigma^0}(\mathbf{P}) \hat{\mathbf{p}} \quad (5b)$$

² The spin four-vector in the rest frame is $S^\mu = (0, \mathbf{S}_*^{(M)})$.

Fig. 2 Comparison between model and experimental data with GLISSANDO initial conditions. Left panels correspond to Au–Au collisions at $\sqrt{s_{NN}} = 200$ GeV at RHIC and the right ones to $\sqrt{s_{NN}} = 5020$ GeV Pb–Pb collisions at LHC. In the upper panels, we show the pseudo-rapidity distribution of charged hadrons, the mid-panels show the elliptic flow of charged hadrons, and the lower panels show the transverse momentum spectrum of charged hadrons. The data are taken from the same references as in Fig. 1



where $\mathbf{S}_{*\Sigma^*}$ and $\mathbf{S}_{*\Sigma^0}$ are the spin vectors of the mother particles in the mother’s rest frame, which can be computed with eEq. (3). The function $F(\mathbf{p}, \Omega_*)$ is given by:

$$F(\mathbf{p}, \Omega_*) = \frac{m_\Lambda^3 (\varepsilon_{*\Lambda} + \varepsilon_\Lambda) \left[(\varepsilon_{*\Lambda} + \varepsilon_\Lambda)^2 - (\varepsilon_\Lambda \varepsilon_{*\Lambda} + \mathbf{p} \cdot \mathbf{p}_* + m_\Lambda^2) \right]}{\varepsilon_{*\Lambda} (\varepsilon_\Lambda \varepsilon_{*\Lambda} + \mathbf{p} \cdot \mathbf{p}_* + m_\Lambda^2)^3}, \quad (6)$$

where $\varepsilon_{*\Lambda}$ and \mathbf{p}_* are the energy and the momentum of the Λ particle in the mother’s rest frame. Finally, the function $n(\mathbf{P})$ is the momentum spectrum of M in the QGP frame obtained from the Cooper–Frye prescription:

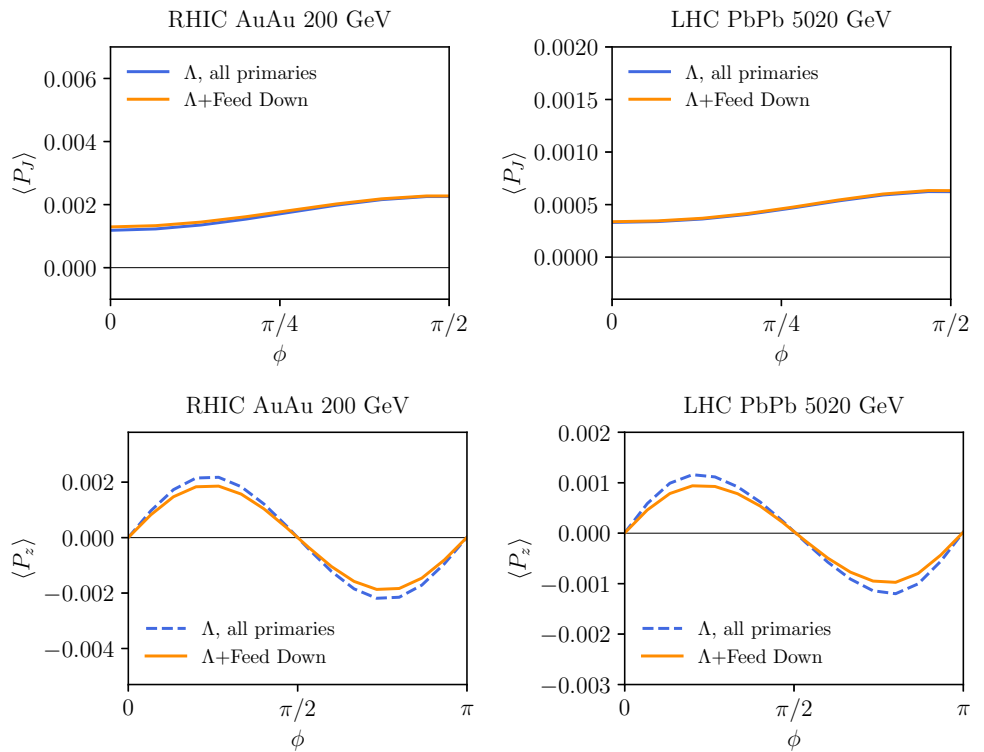
$$n(\mathbf{P}) = \frac{dN}{d^3P} = \frac{1}{\varepsilon_P} \int d\Sigma \cdot P \frac{1}{e^{\beta \cdot P - \mu/T} + 1}. \quad (7)$$

All the integrals in Eq. (4) are evaluated in the hydro-foil code.

To determine the overall Λ ’s polarization, one should know the fraction of primary Λ s and those from the considered decays. Although such fractions are, in principle, momentum dependent, here, for simplicity, we assume that they are constant and use the numbers quoted in Ref. [53] estimated by using the statistical hadronization model: the fraction of primary Λ , at very high energy, is $f_P = 0.243$ whereas for the secondary Λ one has respectively $f_{\Sigma^*} = 0.359$ and $f_{\Sigma^0} = 0.275 \times 0.6 = 0.165$, where the 0.6 takes into account that only $\approx 60\%$ of the Σ^0 are primary; other sources are neglected. Finally, the total Λ ’s spin vector in its rest frame is calculated by normalizing it accordingly:

$$\mathbf{S}_*^{\text{tot}}(p) = \frac{f_P \mathbf{S}_*^P(\mathbf{p}) + f_{\Sigma^*} \mathbf{S}_*^{(\Sigma^*)}(\mathbf{p}) + f_{\Sigma^0} \mathbf{S}_*^{(\Sigma^0)}(\mathbf{p})}{f_P + f_{\Sigma^*} + f_{\Sigma^0}}, \quad (8)$$

Fig. 3 Feed-down corrections on the polarization along the angular momentum direction (upper panels) and along the beam line (lower panels). The solid line shows the polarization including the contribution of Σ^* and Σ^0 while the dashed line shows the calculated polarization assuming that all Λ s are primaries. The simulations are in the centrality window 20–60% for RHIC and 30–50% for LHC



where $S_*^P(\mathbf{p})$ is the spin polarization vector of primary Λ s, determined by boosting the spin vector in the Eq. (1) back to the Λ rest frame and $S_*^{(\Sigma^*)}(\mathbf{p})$, $S_*^{(\Sigma^0)}(\mathbf{p})$ are calculated by means of the Eq. (4).

Figure 3 shows the effect of the feed-down contribution to the component of the polarization vector along the angular momentum (henceforth referred to as *transverse*) and along the beamline (henceforth referred to as *longitudinal*) $\langle P_{J,z} \rangle = 2\langle S_{J,z} \rangle$ by comparing it to a calculation where all Λ are assumed to be primary. The simulations are performed with the `superMC` initial conditions. As already remarked in [52, 53] the combination in (8) results in an accidental approximate cancellation so that the total polarization is almost the same as though the Λ s were only primary. More precisely, the feed-down correction implies a $\approx 10\%$ reduction to the full primary case for the longitudinal component and $\approx 3\%$ for the transverse component. So, even with the contribution from the thermal shear tensor included, which was not the case in Refs. [52, 53], we confirm the previous conclusion that adding feed-down corrections does not significantly change the polarization with respect to the simple assumption of an entirely primary production.

4 Polarization at very high energy: results

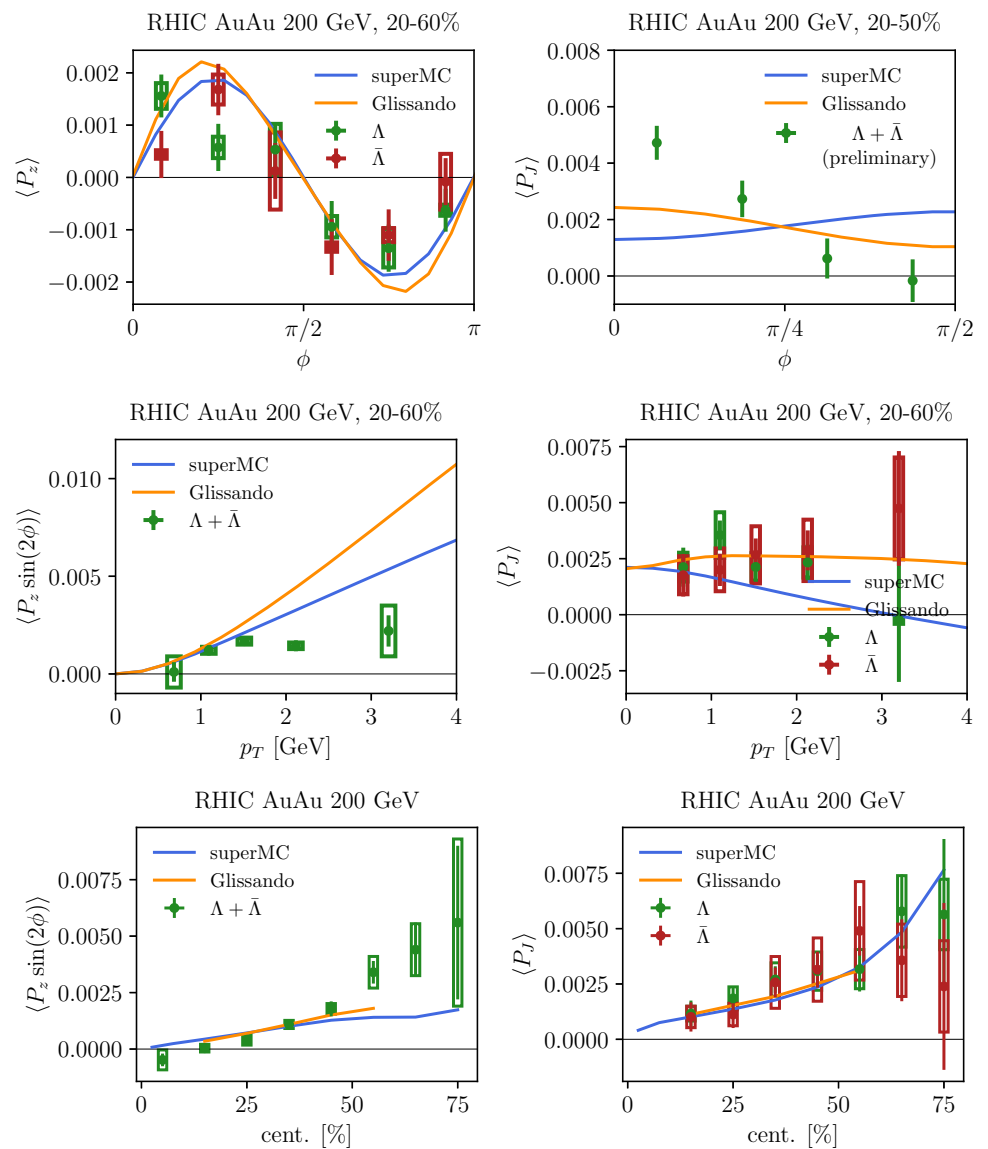
We will now present the results of our calculation and their comparison with the data. In our calculations, feed-down corrections are always included; even though they are small

corrections to the assumption of pure primary production, they certainly improve the accuracy of theoretical predictions. In the plots, we show the proper polarization vector $P^\mu(p) = S_*^\mu(p)/S$ where S is the spin of the particles and $S_*^\mu(p)$ is the mean spin vector in the Λ 's rest frame (hence, for Λ hyperon $P^\mu = 2S_*^\mu$). The value of the Λ decay constant has been set to $\alpha_\Lambda = 0.732$ to compare with experiments [55].

Simulations have been carried out using averaged initial states, which, as has been discussed in Sect. 2, were defined by the models `superMC` and `GLISSANDO`. For the `superMC` IS, the initial state was generated by averaging 20k samples. For `GLISSANDO` IS, 2k–15k samples were used, depending on centrality. We conduct the study with event-averaged initial states, to show generic effects of bulk viscosity on polarization observables. We note that, in an event-by-event fluid dynamic description, a fluctuating and spiky initial state will result in a stronger radial flow, which will need to be compensated by a larger bulk viscosity in order for the mean p_T to agree with an experimentally measured value. Therefore in a more realistic event-by-event simulation, we expect the effects of bulk viscosity to be even larger than in the present study.

In all cases, we compute polarization of Λ s in the rapidity window $\eta \in [-1, 1]$ to match experimental measurements. Polarization as a function of the azimuthal angle $\langle P_z(\phi) \rangle$ and $\langle P_J(\phi) \rangle$ are integrated over the p_T range (0, 6) GeV weighted by the Λ spectrum, whereas $\langle P_z \sin 2\phi \rangle$ is the mean over the azimuthal angle ϕ .

Fig. 4 Comparison between theoretical calculations and experimental data for Au–Au collisions at 200 GeV. Top panels: azimuthal angle dependence of longitudinal and transverse polarization. The middle panels show the transverse momentum dependence of $\langle P_z \sin(2\phi) \rangle$ and $\langle P_J \rangle$, and the bottom panels show their dependence on centrality. For the top and middle panels, the simulations are carried in the centrality 20–60%. The data are taken from Refs. [56–58]



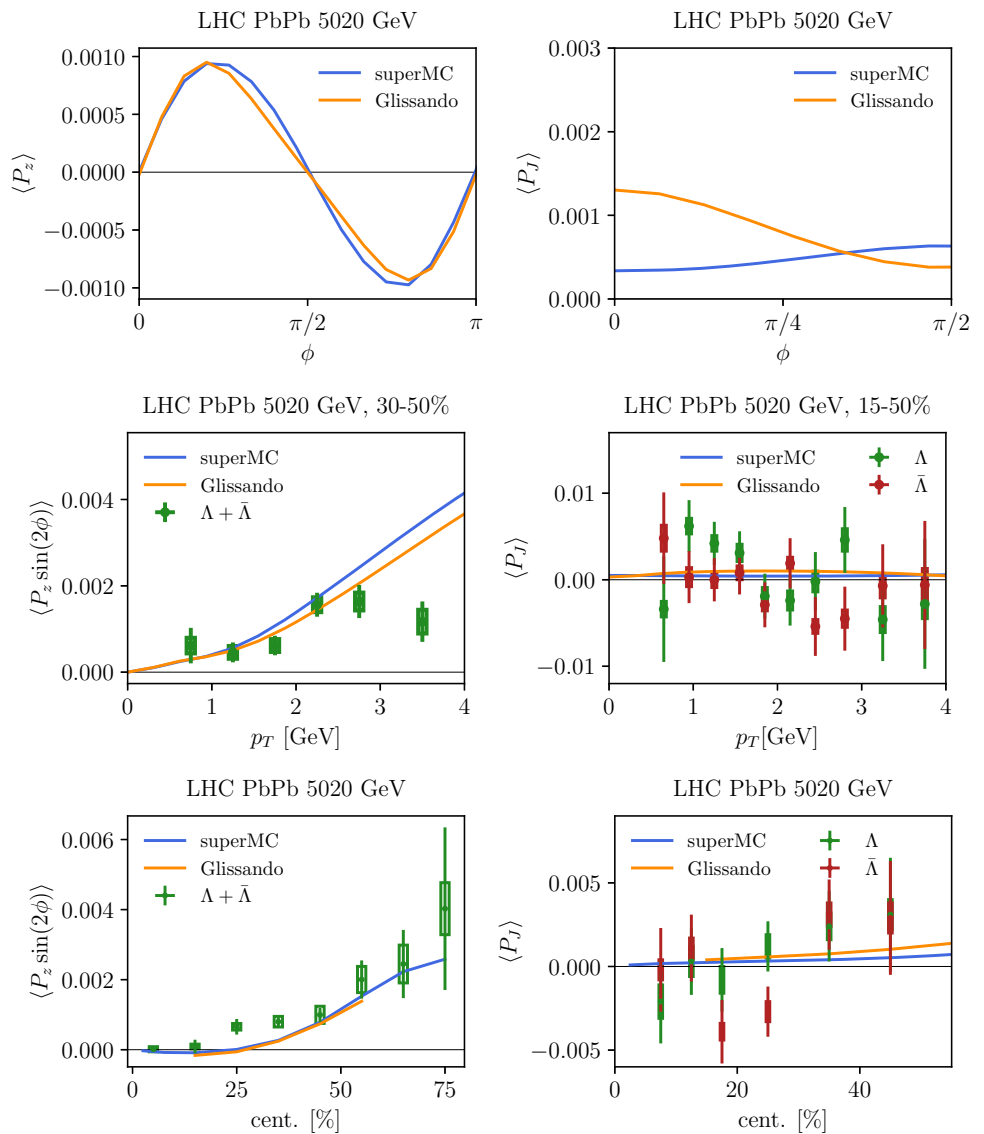
For $\sqrt{s_{NN}} = 200$ GeV Au–Au collisions, the results are shown in Fig. 4 where the data points have been taken from Refs. [56–58]. The centrality reported in the titles in the top and middle panels refers to the data, whereas simulations have always been carried out at 20–60%. Our model describes well the longitudinal component of polarization P_z , as can be seen in the figures, although we overshoot the data in the high p_T region. This result confirms the previous finding [13] that the formula (1) reproduces the data, essentially solving the so-called polarization sign puzzle. The difference between our calculations and those in Ref. [12] using the same initial conditions `superMC` is owing to the use of the isothermal hadronization assumption as well as a difference in the expression of energy ε in (1), which is $p \cdot \hat{t}$ in our case and $p \cdot u$ in Ref. [12].

While `GLISSANDO` and `superMC` provide similar predictions for the longitudinal polarization, they differ for the transverse component and especially for its azimuthal angle

dependence. `GLISSANDO IS` predicts the correct dependence of $\langle P_J \rangle$ on the azimuthal angle. Instead, `superMC` does not get the slope right, although the global polarization (middle-right panel) is well reproduced; similar observations were reported in [12] which, as has been mentioned, used the same IS model. In general, as it can be seen in the other plots in Fig. 4 `GLISSANDO` predicts a larger P_J than `superMC` as a function of p_T and centrality.

A substantial difference in the implementation of longitudinal hydrodynamic initial conditions causes the discrepancy between `GLISSANDO` and `superMC` in the transverse component P_J . Indeed, it should be stressed that the transverse component of the polarization is sensitive to the longitudinal velocity (see the Eq. (1)) whereas the longitudinal component of the polarization is sensitive to the transverse velocity [17,61,62]. While the hydrodynamic initial conditions in the transverse plane are strongly constrained by the observed transverse momentum spectra and their azimuthal

Fig. 5 Comparison between theoretical calculations and experimental data for Pb–Pb collisions at 5020 GeV. Top panels: azimuthal angle dependence of transverse and longitudinal polarization. The middle panels show the transverse momentum dependence of $\langle P_z \sin(2\phi) \rangle$ and $\langle P_J \rangle$, and the bottom panels show their dependence on centrality. For the top and middle panels, the simulations are carried in the centrality 30–50%. The data are taken from Refs. [59,60]



anisotropies, initial longitudinal flow conditions are not accurately known. Indeed, *superMC* IS parametrization entails a non-vanishing τ – η component of the energy-momentum tensor, hence a non-vanishing initial longitudinal velocity, $u^\eta \neq 0$, whereas *GLISSANDO* IS initializes $u^\eta = 0$. This difference will be addressed in more detail in the next section.

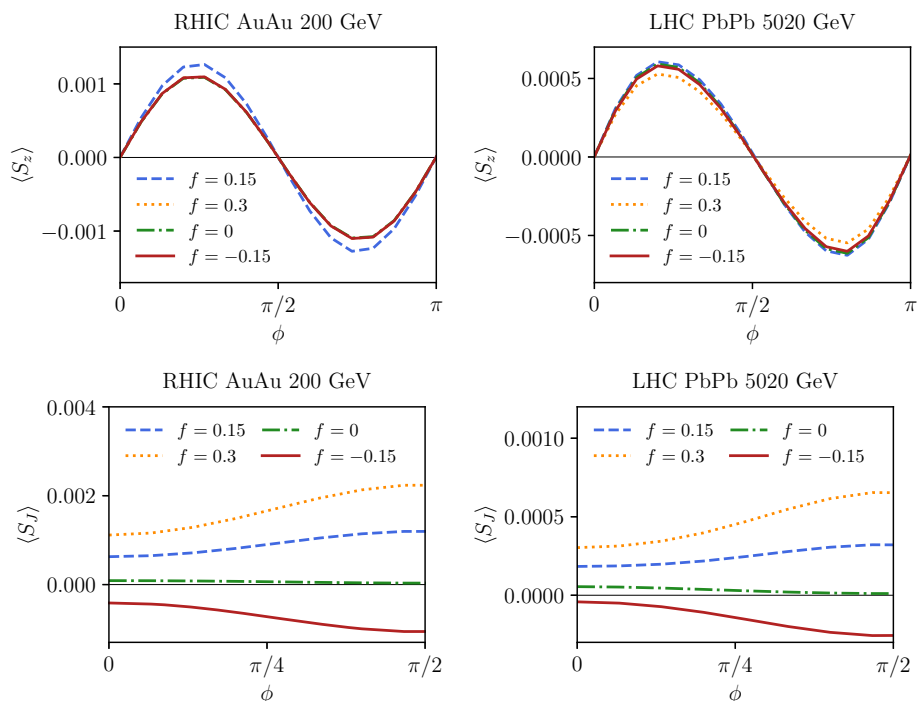
The results of our calculations for Pb–Pb collisions at $\sqrt{s_{NN}} = 5020$ GeV are shown in Fig. 5 along with the ALICE data [59,60]. The top panels show the theoretical predictions of longitudinal and transverse polarization as a function of the azimuthal angle: no data is available for these observables yet. In the middle panels, once again, the centrality reported in the title refers to the data, whereas simulations have been carried out at 30–50%. The predicted longitudinal polarization is smaller than at RHIC energy by a factor of ≈ 2 with both IS conditions. It can be seen that our calculations for the longitudinal polarization with both IS models agree with each other, as well as with the data (when available). On the

other hand, like at RHIC energy, the predictions of the two IS models used are very different for the transverse polarization. The measurement of P_J at this energy has significantly larger error bars than RHIC energy, so no definite conclusion can be drawn from comparing the predictions with the data.

5 Sensitivity to initial conditions and transport coefficients

In this section, we delve into the capability of spin polarization as a probe of the hydrodynamic initial conditions and the transport coefficients of the QGP. We already mentioned that the two IS used differ in the predictions of the transverse polarization P_J , which reflects different initial conditions for the longitudinal momentum density. To make this apparent, we have studied the sensitivity of $P_z(\phi)$ and $P_J(\phi)$ to the parameter f in the *superMC* IS model. This parameter

Fig. 6 Azimuthal angle dependence of S_z (upper panels) and S_J (lower panels) for different values of the parameter f in the superMC initial state model. RHIC simulations are made in 20–60% centrality, whereas LHC at 30–50%



determines the initial values of the components of the energy-momentum tensor in the Milne coordinates as follows:

$$T^{\tau\tau} = \rho \cosh(f y_{CM}) \tag{9a}$$

$$T^{\tau\eta} = \frac{\rho}{\tau} \sinh(f y_{CM}) \tag{9b}$$

where ρ is the local energy density distribution and y_{CM} is the center of mass rapidity (for a full description of these quantities, see Ref. [12]). Therefore, the value of f characterizes the initial longitudinal momentum density $T^{\tau\eta}$, thus driving the initial longitudinal flow and the fireball’s total angular momentum. The latter affects the transverse component of the polarization P_J as already discussed. We note that the Eq. (9) have been considered also in Ref. [17], where the dependence on f of the Λ polarization has been studied at $\sqrt{s_{NN}} = 27$ GeV. Figure 6 shows both transverse and longitudinal polarization from hydrodynamic simulations of Au–Au and Pb–Pb collisions initialized with different values of f . As expected, while the longitudinal component is almost insensitive to f , the transverse component changes significantly in magnitude, slope, and even sign. This sensitivity makes it possible to use local transverse polarization to discriminate between different models of initial longitudinal conditions and to pin down the amount of initial longitudinal momentum density. For the case at hand, the curves are shown in Fig. 6, and the results from GLISSANDO IS presented in the Sect. 4 seem to favor the option $u^\eta = 0$, implemented by $f = 0$, which is the only one yielding at least the correct sign of the slope of the function $P_J(\phi)$ at RHIC.

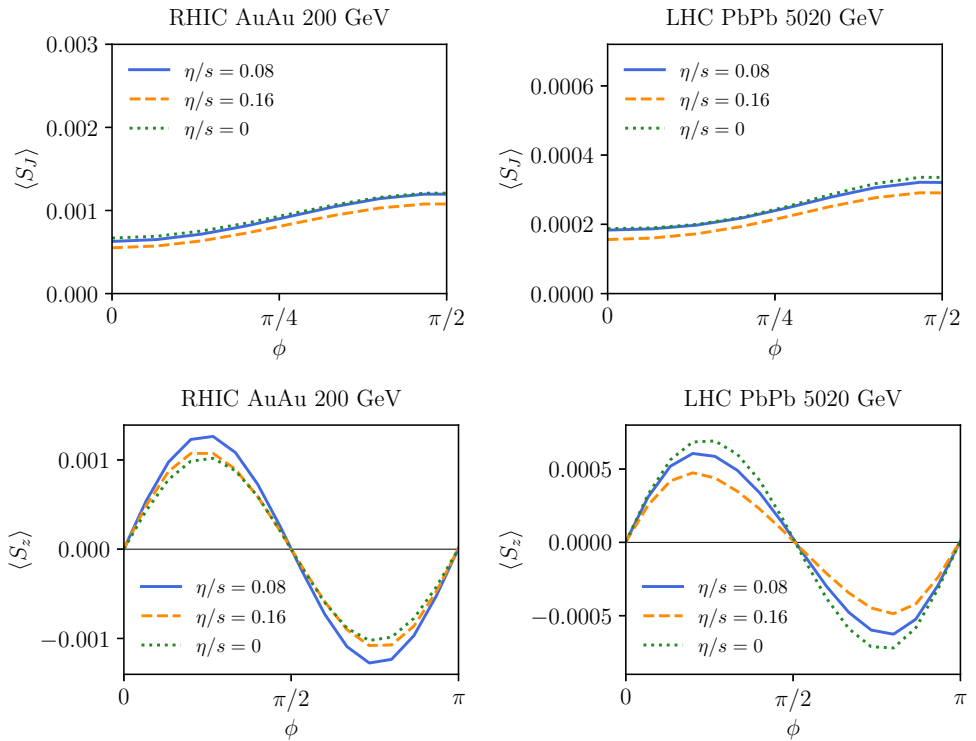
We have also studied the dependence of the polarization on the shear viscosity and the bulk viscosity. In Fig. 7, the transverse and longitudinal components of the spin vector of primary Λ s with the superMC IS, averaged over the same kinematic intervals as in Sect. 4, are shown at RHIC and LHC energies for different constant ratios of η/s whereas the bulk viscosity is given by the parametrization III as explained in Sect. 2. The transverse component is almost insensitive to the shear viscosity, while the longitudinal component has a limited sensitivity. Interestingly, we notice that while at RHIC energies, a larger viscosity enhances the signal, at LHC, it slightly reduces it.

Conversely, bulk viscosity has a sizeable effect on polarization, especially at high energy, in agreement with previous observations [63]. We have used three different parametrizations of bulk viscosity as a function of temperature [64]. The first one, dubbed as “Parametrization I” was introduced in Ref. [65]:

$$\zeta/s = \begin{cases} c_1 + 0.08 \exp\left[\frac{T/T_p - 1}{0.0025}\right] + 0.22 \exp\left[\frac{T/T_p - 1}{0.0022}\right] & T < T_p \\ c_2 + 27.55 (T/T_p) - 13.77 (T/T_p)^2 & T_p < T < T_P \\ c_3 + 0.9 \exp\left[\frac{-(T/T_p - 1)}{0.0025}\right] + 0.25 \exp\left[\frac{-(T/T_p - 1)}{0.13}\right] & T > T_P, \end{cases} \tag{10}$$

where $T_p = 180$ MeV, $T_P = 200$ MeV, $c_1 = 0.03$, $c_2 = -13.45$ and $c_3 = 0.001$. The second parametrization was introduced in Ref. [66]:

Fig. 7 Transverse and longitudinal components of the spin vector as a function of the azimuthal angle ϕ for various values of the shear viscosity over entropy density. The centrality window is 20–60% for RHIC and 30–50% for LHC



$$\zeta/s = \begin{cases} B_{\text{norm}} \exp \left[- \left(\frac{T - T_{\text{peak}}}{T_{\text{width}}} \right)^2 \right] & T < T_{\text{peak}} \\ B_{\text{norm}} \frac{B_{\text{width}}^2}{(T/T_{\text{peak}} - 1)^2 + B_{\text{width}}^2} & T > T_{\text{peak}}, \end{cases} \quad (11)$$

where $T_{\text{peak}} = 165$ MeV, $B_{\text{norm}} = 0.24$, $B_{\text{width}} = 1.5$ and $T_{\text{width}} = 50$ MeV. The last parametrization, dubbed as ‘‘Parametrization III’’, was introduced in Ref. [49] and it reads:

$$\zeta/s = \begin{cases} B_n \exp \left[- \left(\frac{T - T_\mu}{B_1} \right)^2 \right] & T < T_\mu \\ B_n \exp \left[- \left(\frac{T - T_\mu}{B_2} \right)^2 \right] & T > T_\mu, \end{cases} \quad (12)$$

where $B_n = 0.13$, $B_1 = 10$ MeV, $B_2 = 120$ MeV and $T_\mu = 160$ MeV. These parametrizations are shown in Fig. 8, where it can be seen that parametrization I has the sharpest peak around the transition temperature, the other two featuring a broader peak. In parametrization II, ζ/s is always larger than parametrization III.

The components of the mean spin vector - of primary particles only - along the angular momentum direction and the beam axis are shown in Fig. 9 in Au–Au collisions at $\sqrt{s_{\text{NN}}} = 200$ GeV and Pb–Pb collisions at $\sqrt{s_{\text{NN}}} = 5020$ GeV for all the different parametrizations and using the `superMC` IS (with $f = 0.15$ as in the initial tuning). Bulk viscosity’s effect on polarization is mild at $\sqrt{s_{\text{NN}}} = 200$ GeV: different parametrizations slightly change the magnitude of the polarization signal compared to the case of $\zeta = 0$, but their difference is well within the experimental

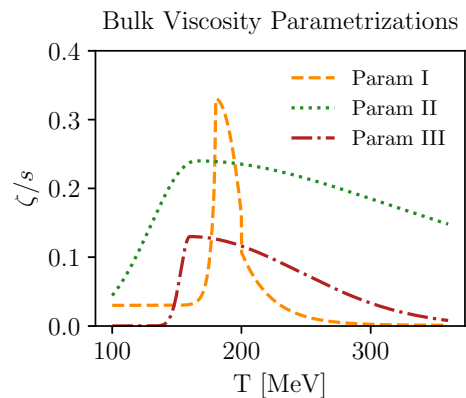
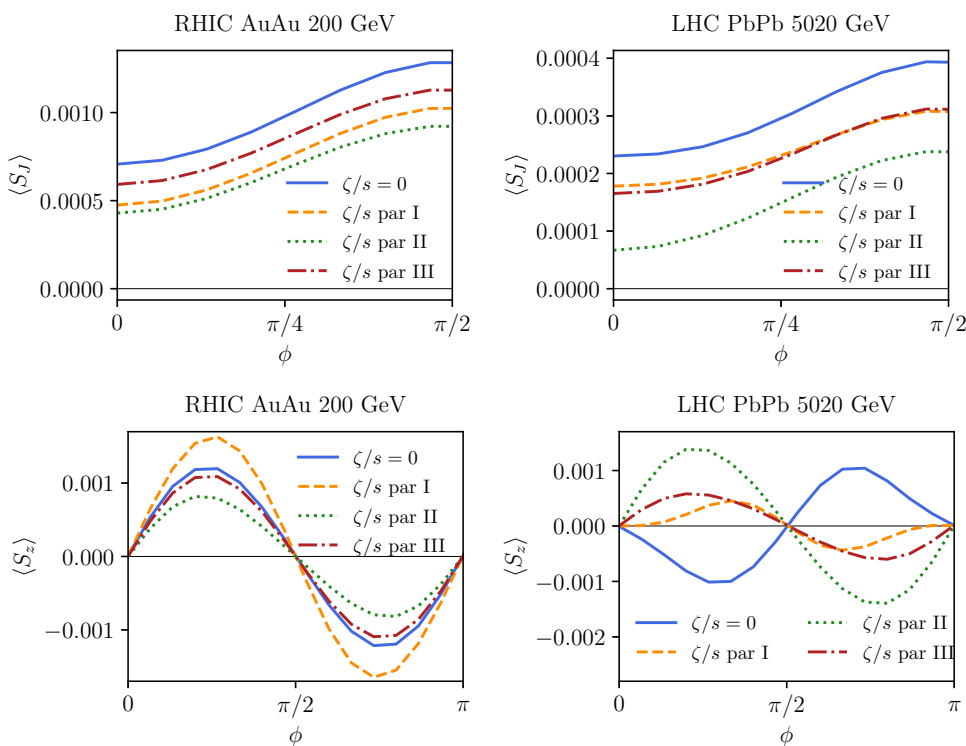


Fig. 8 The temperature dependence of the bulk viscosity over entropy density ratio is used in this work

errors. Instead, surprisingly, at $\sqrt{s_{\text{NN}}} = 5020$ GeV the effect of bulk viscosity is dramatic: the longitudinal polarization flips/changes sign when bulk viscosity is introduced, and the difference between the three parametrizations is large. Identifying a single effect responsible for such different behavior at RHIC and LHC energies is hard. A possible explanation could be that the higher average temperature and the longer lifetime of the QGP at the LHC energy make the role of bulk viscosity more important.

To investigate this phenomenon in more detail, we have computed the contribution of different hydrodynamic gradients to the spin vector for primary Λ s. Referring to Eq. (1), the kinematic vorticity and shear can be decomposed in terms of acceleration $A^\mu = u \cdot \partial u^\mu$, angular veloc-

Fig. 9 Transverse and longitudinal components of the spin vector as a function of the azimuthal angle ϕ for various bulk viscosity parametrization at $\sqrt{s_{NN}} = 200$ GeV (20–60% centrality) and $\sqrt{s_{NN}} = 5020$ GeV (30–50% centrality). For these plots we used the superMC initial state



ity $\omega^\mu = -1/2 \epsilon^{\mu\nu\rho\sigma} \partial_\rho u_\nu u_\sigma$, shear stress tensor $\sigma^{\mu\nu}$ and expansion scalar θ so that:

$$\omega_{\mu\nu} = \epsilon_{\mu\nu\rho\sigma} \omega^\rho u^\sigma + \frac{1}{2} (A_\mu u_\nu - A_\nu u_\mu), \tag{13}$$

$$\Xi_{\mu\nu} = \frac{1}{2} (A_\mu u_\nu + A_\nu u_\mu) + \sigma_{\mu\nu} + \frac{1}{3} \theta \Delta_{\mu\nu}, \tag{14}$$

where $\Delta^{\mu\nu} = g^{\mu\nu} - u^\mu u^\nu$. Defining $\nabla_\mu = \Delta_{\mu\nu} \partial^\nu$, one has:

$$\theta = \nabla \cdot u = \partial \cdot u,$$

$$\sigma_{\mu\nu} = \frac{1}{2} (\nabla_\mu u_\nu + \nabla_\nu u_\mu) - \frac{1}{3} \theta \Delta_{\mu\nu}.$$

By decomposing the tensors $\omega_{\mu\nu}$ and $\Xi_{\mu\nu}$ in the formula (1) according to the above equations it is possible to identify different contributions to the spin polarization vector:

$$S_{A_\omega}^\mu = -\epsilon^{\mu\nu\rho\sigma} p_\sigma \frac{\int_\Sigma d\Sigma \cdot p n_F (1 - n_F) A_\nu u_\rho}{8mT_H \int_\Sigma d\Sigma \cdot p n_F}, \tag{15a}$$

$$S_\omega^\mu = \frac{\int_\Sigma d\Sigma \cdot p n_F (1 - n_F) [\omega^\mu u \cdot p - u^\nu \omega \cdot p]}{4mT_H \int_\Sigma d\Sigma \cdot p n_F}, \tag{15b}$$

$$S_{A_\Xi}^\mu = -\epsilon^{\mu\rho\sigma\tau} \hat{t}_\rho p_\tau \frac{\int_\Sigma d\Sigma \cdot p n_F (1 - n_F) [u_\sigma A \cdot p + A_\sigma u \cdot p]}{8mT_H \int_\Sigma d\Sigma \cdot p n_F}, \tag{15c}$$

$$S_\sigma^\mu = -\epsilon^{\mu\rho\sigma\tau} \hat{t}_\rho p_\tau \frac{p^\lambda \int_\Sigma d\Sigma \cdot p n_F (1 - n_F) \sigma_{\lambda\sigma}}{4mT_H \int_\Sigma d\Sigma \cdot p n_F}, \tag{15d}$$

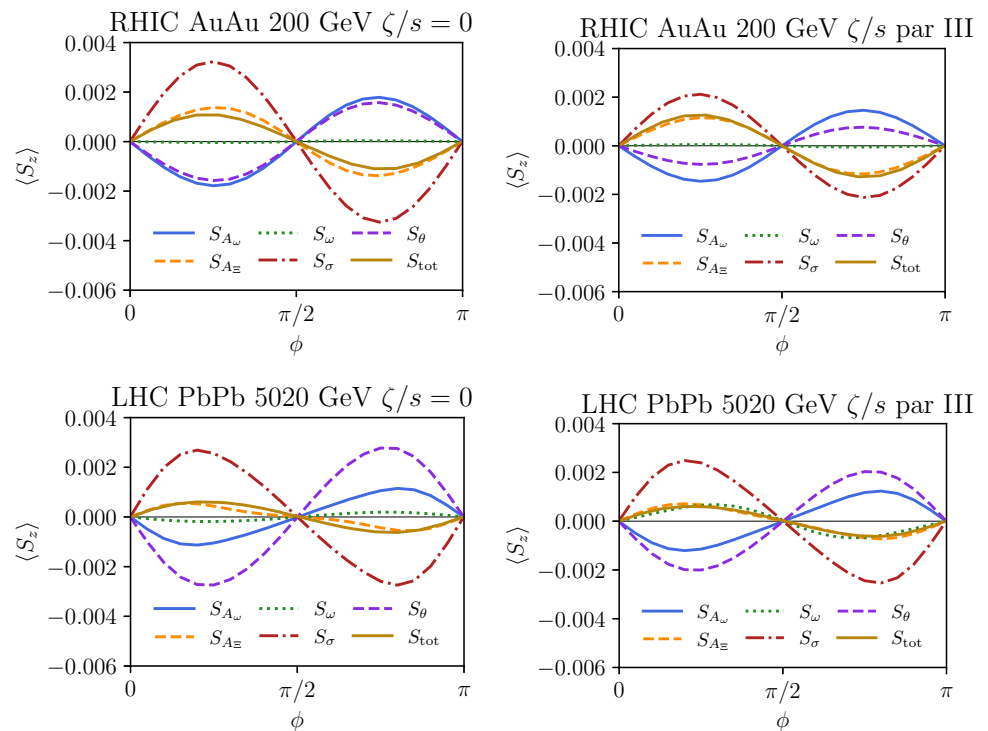
$$S_\theta^\mu = -\epsilon^{\mu\rho\sigma\tau} \hat{t}_\rho p_\tau \frac{p^\lambda \int_\Sigma d\Sigma \cdot p n_F (1 - n_F) \theta \Delta_{\lambda\sigma}}{12mT_H \int_\Sigma d\Sigma \cdot p n_F}. \tag{15e}$$

We have computed the above components for two bulk viscosities: parametrization III of ζ/s in Eq. (12) and for vanishing $\zeta/s = 0$, see Fig. 10. In Au–Au collisions at RHIC energy, the contribution from angular velocity is almost vanishing, according to previous findings [67] and contrary to the naive lore, which identifies rotation as the main source of polarization. Overall, for parametrization III, the amplitude of both S_σ and S_θ is smaller than for $\zeta = 0$ case, but their sum is approximately zero and the total polarization is almost unaffected. On the other hand, in Pb–Pb collisions at LHC energy, the situation is more complicated. Without bulk viscosity, S_θ seemingly cancels S_σ , and S_{A_Ξ} dictates the (negative) sign of the polarization harmonic. Turning on the bulk viscosity, not only do S_θ and S_σ get smaller in magnitude, but also S_ω and S_{A_Ξ} significantly change, resulting in the change of sign of the oscillation pattern.

6 Conclusions

In summary, we have presented an analysis of spin polarization of Λ produced in Au–Au collisions at $\sqrt{s_{NN}} = 200$ GeV and in Pb–Pb collisions at $\sqrt{s_{NN}} = 5020$ GeV, using two different initial state models. By assuming that the particlezation hypersurface is isothermal and including the feed-down corrections, we have found a good agreement between the data and the predictions of the hydrodynamic-statistical model, thus confirming the previous finding [13] that isothermal assumption is an important point to reproduce the data. Calculations with GLISSANDO initial state model are in

Fig. 10 Contributions to the spin polarization vector (see Eq. 15), for primary Λ 's at RHIC (centrality window 20–60%), and LHC energy (centrality window 30–50%)



good agreement with the data while `superMC` initial state model reproduces the longitudinal component and the global transverse polarization but fails to reproduce the transverse polarization as a function of the azimuthal angle. Transverse polarization is very sensitive to the initial longitudinal flow, and our results seem to favor a scenario with initial boost-invariant flow velocity.

We have shown that the longitudinal polarization is very sensitive to bulk viscosity at the highest collision energy and almost insensitive to the shear viscosity. At the LHC energy, the presence of bulk viscosity flips the sign of the polarization along the beam direction compared to a scenario with ideal fluid evolution.

Altogether, these results demonstrate that spin polarization, and in particular its azimuthal angle dependence, can be used as a very effective probe of initial conditions and transport coefficients of the quark–gluon plasma.

Acknowledgements We are greatly indebted with C. Shen for his help with the comparison of our results with his. This work is supported by ICSC - *Centro Nazionale di Ricerca in High Performance Computing, Big Data and Quantum Computing*, funded by European Union - NextGenerationEU and by the project PRIN2022 *Advanced Probes of the Quark Gluon Plasma* funded by "Ministero dell'Università e della Ricerca". A.P. is supported by the U.S. Department of Energy under Grants DE-FG88ER40388. I.K. acknowledges support by the Czech Science Foundation under project No. 22-25026 S. Computational resources were provided by the e-INFRA CZ project (ID:90254), supported by the Ministry of Education, Youth and Sports of the Czech Republic.

Data Availability Statement Data will be made available on reasonable request. [Authors' comment: The datasets generated during and/or

analysed during the current study are available from the corresponding author on reasonable request.]

Code Availability Statement This manuscript has associated code/software in a data repository. [Authors' comment: The new code developed for this publication is publicly available at <https://github.com/fafafrens/smash-vhllh-hybrid-python> and <https://github.com/AndrePalermo/hydro-foil>.]

Open Access This article is licensed under a Creative Commons Attribution 4.0 International License, which permits use, sharing, adaptation, distribution and reproduction in any medium or format, as long as you give appropriate credit to the original author(s) and the source, provide a link to the Creative Commons licence, and indicate if changes were made. The images or other third party material in this article are included in the article's Creative Commons licence, unless indicated otherwise in a credit line to the material. If material is not included in the article's Creative Commons licence and your intended use is not permitted by statutory regulation or exceeds the permitted use, you will need to obtain permission directly from the copyright holder. To view a copy of this licence, visit <http://creativecommons.org/licenses/by/4.0/>.

Funded by SCOAP³.

References

1. L. Adamczyk et al. (STAR), *Nature* **548**, 62 (2017). <https://doi.org/10.1038/nature23004>. arXiv:1701.06657 [nucl-ex]
2. F. Becattini, M.A. Lisa, *Annu. Rev. Nucl. Part. Sci.* **70**, 395 (2020). <https://doi.org/10.1146/annurev-nucl-021920-095245>. arXiv:2003.03640 [nucl-ex]
3. F. Becattini, *Rep. Prog. Phys.* **85**, 122301 (2022). <https://doi.org/10.1088/1361-6633/ac97a9>. arXiv:2204.01144 [nucl-th]
4. F. Becattini, M. Buzzegoli, T. Niida, S. Pu, A.-H. Tang, Q. Wang, (2024). arXiv:2402.04540 [nucl-th]

5. F. Becattini, V. Chandra, L. Del Zanna, E. Grossi, *Ann. Phys.* **338**, 32 (2013). <https://doi.org/10.1016/j.aop.2013.07.004>. arXiv:1303.3431 [nucl-th]
6. R.-H. Fang, L.-G. Pang, Q. Wang, X.-N. Wang, *Phys. Rev. C* **94**, 024904 (2016). <https://doi.org/10.1103/PhysRevC.94.024904>. arXiv:1604.04036 [nucl-th]
7. W. Florkowski, A. Kumar, R. Ryblewski, *Phys. Rev. C* **98**, 044906 (2018). <https://doi.org/10.1103/PhysRevC.98.044906>. arXiv:1806.02616 [hep-ph]
8. N. Weickgenannt, E. Speranza, X.-L. Sheng, Q. Wang, D.H. Rischke, *Phys. Rev. Lett.* **127**, 052301 (2021). <https://doi.org/10.1103/PhysRevLett.127.052301>. arXiv:2005.01506 [hep-ph]
9. F. Becattini, M. Buzzegoli, A. Palermo, *Phys. Lett. B* **820**, 136519 (2021). <https://doi.org/10.1016/j.physletb.2021.136519>. arXiv:2103.10917 [nucl-th]
10. S.Y.F. Liu, Y. Yin, *JHEP* **07**, 188 (2021). [https://doi.org/10.1007/JHEP07\(2021\)188](https://doi.org/10.1007/JHEP07(2021)188). arXiv:2103.09200 [hep-ph]
11. C. Yi, S. Pu, D.-L. Yang, *Phys. Rev. C* **104**, 064901 (2021). <https://doi.org/10.1103/PhysRevC.104.064901>. arXiv:2106.00238 [hep-ph]
12. S. Alzhrani, S. Ryu, C. Shen, *Phys. Rev. C* **106**, 014905 (2022). <https://doi.org/10.1103/PhysRevC.106.014905>. arXiv:2203.15718 [nucl-th]
13. F. Becattini, M. Buzzegoli, G. Inghirami, I. Karpenko, A. Palermo, *Phys. Rev. Lett.* **127**, 272302 (2021). <https://doi.org/10.1103/PhysRevLett.127.272302>. arXiv:2103.14621 [nucl-th]
14. B. Fu, S.Y.F. Liu, L. Pang, H. Song, Y. Yin, *Phys. Rev. Lett.* **127**, 142301 (2021). <https://doi.org/10.1103/PhysRevLett.127.142301>. arXiv:2103.10403 [hep-ph]
15. X.-Y. Wu, C. Yi, G.-Y. Qin, S. Pu, *Phys. Rev. C* **105**, 064909 (2022). <https://doi.org/10.1103/PhysRevC.105.064909>. arXiv:2204.02218 [hep-ph]
16. Z.-F. Jiang, X.-Y. Wu, H.-Q. Yu, S.-S. Cao, B.-W. Zhang, *Acta Phys. Sin.* **72**, 072504 (2023). <https://doi.org/10.7498/aps.72.20222391>
17. Z.-F. Jiang, X.-Y. Wu, S. Cao, B.-W. Zhang, *Phys. Rev. C* **108**, 064904 (2023). <https://doi.org/10.1103/PhysRevC.108.064904>. arXiv:2307.04257 [nucl-th]
18. V.H. Ribeiro, D. Dobrigkeit Chinellato, M.A. Lisa, W. Mantioli Serenone, C. Shen, J. Takahashi, G. Torrieri, *Phys. Rev. C* **109**, 014905 (2024). <https://doi.org/10.1103/PhysRevC.109.014905>. arXiv:2305.02428 [hep-ph]
19. C. Shen, Private communication
20. H.-Z. Wu, L.-G. Pang, X.-G. Huang, Q. Wang, *Phys. Rev. Res.* **1**, 033058 (2019). <https://doi.org/10.1103/PhysRevResearch.1.033058>. arXiv:1906.09385 [nucl-th]
21. W. Florkowski, A. Kumar, R. Ryblewski, A. Mazeliauskas, *Phys. Rev. C* **100**, 054907 (2019). <https://doi.org/10.1103/PhysRevC.100.054907>. arXiv:1904.00002 [nucl-th]
22. X.-G. Huang, J. Liao, Q. Wang, X.-L. Xia, *Lect. Notes Phys.* **987**, 281 (2021). https://doi.org/10.1007/978-3-030-71427-7_9. arXiv:2010.08937 [nucl-th]
23. A. Lei, D. Wang, D.-M. Zhou, B.-H. Sa, L.P. Csernai, *Phys. Rev. C* **104**, 054903 (2021). <https://doi.org/10.1103/PhysRevC.104.054903>. arXiv:2110.13485 [nucl-th]
24. W.M. Serenone, J.G.P. Barbon, D.D. Chinellato, M.A. Lisa, C. Shen, J. Takahashi, G. Torrieri, *Phys. Lett. B* **820**, 136500 (2021). <https://doi.org/10.1016/j.physletb.2021.136500>. arXiv:2102.11919 [hep-ph]
25. S.K. Singh, J.-E. Alam, *Eur. Phys. J. C* **83**, 585 (2023). <https://doi.org/10.1140/epjc/s10052-023-11776-5>. arXiv:2110.15604 [hep-ph]
26. W. Florkowski, A. Kumar, A. Mazeliauskas, R. Ryblewski, *Phys. Rev. C* **105**, 064901 (2022). <https://doi.org/10.1103/PhysRevC.105.064901>. arXiv:2112.02799 [hep-ph]
27. B. Fu, L. Pang, H. Song, Y. Yin, (2022). arXiv:2201.12970 [hep-ph]
28. C. Yi, X.-Y. Wu, D.-L. Yang, J.-H. Gao, S. Pu, G.-Y. Qin, *Phys. Rev. C* **109**, L011901 (2024). <https://doi.org/10.1103/PhysRevC.109.L011901>. arXiv:2304.08777 [hep-ph]
29. I. Karpenko, P. Huovinen, M. Bleicher, *Comput. Phys. Commun.* **185**, 3016 (2014). <https://doi.org/10.1016/j.cpc.2014.07.010>. arXiv:1312.4160 [nucl-th]
30. A. Schäfer, I. Karpenko, X.-Y. Wu, J. Hammelmann, H. Elfner (SMASH), *Eur. Phys. J. A* **58**, 230 (2022). <https://doi.org/10.1140/epja/s10050-022-00872-x>. arXiv:2112.08724 [hep-ph]
31. D. Oliinychenko, J. Staudenmaier, V. Steinberg, J. Weil, A. Sciarra, A. Schäfer, H.E. Petersen, S. Ryu, J. Mohs, G. Inghirami, F. Li, A. Sorensen, D. Mitrovic, L. Pang, H. Roch, void One, R. Hirayama, O. Garcia-Montero, M. Mayer, N. Kübler, S. Spies, J. Gröbel, N.-U. Bastian, *Smash-transport/smash: Smash-3.0*. (2023). <https://doi.org/10.5281/zenodo.7870822>
32. J. Weil et al. (SMASH), *Phys. Rev. C* **94**, 054905 (2016). <https://doi.org/10.1103/PhysRevC.94.054905>. arXiv:1606.06642 [nucl-th]
33. P. Huovinen, H. Petersen, *Eur. Phys. J. A* **48**, 171 (2012). <https://doi.org/10.1140/epja/i2012-12171-9>. arXiv:1206.3371 [nucl-th]
34. *Smash-transport/smash-hadron-sampler*. (2023). <https://github.com/smash-transport/smash-hadron-sampler/releases/tag/SMASH-hadron-sampler-3.0>
35. *HYDROdynamic Freeze-Out IntegraLs*. Github.com/AndrePalermo/hydro-foil
36. F. Mölder, K.P. Jablonski, B. Letcher, M.B. Hall, C.H. Tomkins-Tinch, V. Sochat, J. Forster, S. Lee, S.O. Twardziok, A. Kanitz, et al., *F1000Research* **10** (2021)
37. *SMASH-vHLLH hybrid with Python*. The repository will be made available upon publication
38. C. Shen, S. Alzhrani, *Phys. Rev. C* **102**, 014909 (2020). <https://doi.org/10.1103/PhysRevC.102.014909>. arXiv:2003.05852 [nucl-th]
39. J. Cimerman, I. Karpenko, B. Tomášik, B.A. Trzeciak, *Phys. Rev. C* **103**, 034902 (2021). <https://doi.org/10.1103/PhysRevC.103.034902>. arXiv:2012.10266 [nucl-th]
40. I.G. Bearden et al. (BRAHMS), *Phys. Rev. Lett.* **88**, 202301 (2002). <https://doi.org/10.1103/PhysRevLett.88.202301>. arXiv:nucl-ex/0112001
41. J. Adam et al. (ALICE), *Phys. Lett. B* **772**, 567 (2017). <https://doi.org/10.1016/j.physletb.2017.07.017>. arXiv:1612.08966 [nucl-ex]
42. J. Adams et al. (STAR), *Phys. Rev. C* **72**, 014904 (2005). <https://doi.org/10.1103/PhysRevC.72.014904>. arXiv:nucl-ex/0409033
43. S. Acharya et al. (ALICE), *JHEP* **05**, 243 (2023). [https://doi.org/10.1007/JHEP05\(2023\)243](https://doi.org/10.1007/JHEP05(2023)243). arXiv:2206.04587 [nucl-ex]
44. J. Adams et al. (STAR), *Phys. Rev. Lett.* **91**, 172302 (2003). <https://doi.org/10.1103/PhysRevLett.91.172302>. arXiv:nucl-ex/0305015
45. S. Acharya et al. (ALICE), *JHEP* **11**, 013 (2018). [https://doi.org/10.1007/JHEP11\(2018\)013](https://doi.org/10.1007/JHEP11(2018)013). arXiv:1802.09145 [nucl-ex]
46. J.S. Moreland, J.E. Bernhard, S.A. Bass, *Phys. Rev. C* **92**, 011901 (2015). <https://doi.org/10.1103/PhysRevC.92.011901>. arXiv:1412.4708 [nucl-th]
47. M. Rybczynski, G. Stefanek, W. Broniowski, P. Bozek, *Comput. Phys. Commun.* **185**, 1759 (2014). <https://doi.org/10.1016/j.cpc.2014.02.016>. arXiv:1310.5475 [nucl-th]
48. P. Bozek, *Phys. Rev. C* **85**, 034901 (2012). <https://doi.org/10.1103/PhysRevC.85.034901>. arXiv:1110.6742 [nucl-th]
49. B. Schenke, C. Shen, P. Tribedy, *Phys. Rev. C* **102**, 044905 (2020). <https://doi.org/10.1103/PhysRevC.102.044905>. arXiv:2005.14682 [nucl-th]
50. P. Bozek, W. Broniowski, A. Olszewski, *Phys. Rev. C* **91**, 054912 (2015). <https://doi.org/10.1103/PhysRevC.91.054912>. arXiv:1503.07425 [nucl-th]
51. F. Becattini, I. Karpenko, M. Lisa, I. Upsal, S. Voloshin, *Phys. Rev. C* **95**, 054902 (2017). <https://doi.org/10.1103/PhysRevC.95.054902>. arXiv:1610.02506 [nucl-th]

52. X.-L. Xia, H. Li, X.-G. Huang, H.Z. Huang, *Phys. Rev. C* **100**, 014913 (2019). <https://doi.org/10.1103/PhysRevC.100.014913>. [arXiv:1905.03120](https://arxiv.org/abs/1905.03120) [nucl-th]
53. F. Becattini, G. Cao, E. Speranza, *Eur. Phys. J. C* **79**, 741 (2019). <https://doi.org/10.1140/epjc/s10052-019-7213-6>. [arXiv:1905.03123](https://arxiv.org/abs/1905.03123) [nucl-th]
54. A. Palermo, F. Becattini, *Eur. Phys. J. Plus* **138**, 547 (2023). <https://doi.org/10.1140/epjp/s13360-023-04169-w>. [arXiv:2304.02276](https://arxiv.org/abs/2304.02276) [nucl-th]
55. P.A. Zyla et al. (Particle Data Group), *PTEP* **2020**, 083C01 (2020). <https://doi.org/10.1093/ptep/ptaa104>
56. T. Niida (STAR), *Nucl. Phys. A* **982**, 511 (2019). <https://doi.org/10.1016/j.nuclphysa.2018.08.034>. [arXiv:1808.10482](https://arxiv.org/abs/1808.10482) [nucl-ex]
57. J. Adam et al. (STAR), *Phys. Rev. C* **98**, 014910 (2018). <https://doi.org/10.1103/PhysRevC.98.014910>. [arXiv:1805.04400](https://arxiv.org/abs/1805.04400) [nucl-ex]
58. J. Adam et al. (STAR), *Phys. Rev. Lett.* **123**, 132301 (2019). <https://doi.org/10.1103/PhysRevLett.123.132301>. [arXiv:1905.11917](https://arxiv.org/abs/1905.11917) [nucl-ex]
59. S. Acharya et al. (ALICE), *Phys. Rev. C* **101**, 044611 (2020). <https://doi.org/10.1103/PhysRevC.101.044611>. [arXiv:1909.01281](https://arxiv.org/abs/1909.01281) [nucl-ex]. [Erratum: *Phys.Rev.C* 105, 029902 (2022)]
60. S. Acharya et al. (ALICE), *Phys. Rev. Lett.* **128**, 172005 (2022). <https://doi.org/10.1103/PhysRevLett.128.172005>. [arXiv:2107.11183](https://arxiv.org/abs/2107.11183) [nucl-ex]
61. F. Becattini, I. Karpenko, *Phys. Rev. Lett.* **120**, 012302 (2018). <https://doi.org/10.1103/PhysRevLett.120.012302>. [arXiv:1707.07984](https://arxiv.org/abs/1707.07984) [nucl-th]
62. S.A. Voloshin, *EPJ Web Conf.* **171**, 07002 (2018). <https://doi.org/10.1051/epjconf/201817107002>. [arXiv:1710.08934](https://arxiv.org/abs/1710.08934) [nucl-ex]
63. A. Palermo, F. Becattini, M. Buzzegoli, G. Inghirami, I. Karpenko, *EPJ Web Conf.* **276**, 01026 (2023). <https://doi.org/10.1051/epjconf/202327601026>. [arXiv:2208.09874](https://arxiv.org/abs/2208.09874) [nucl-th]
64. J. Bobek, I. Karpenko, (2022). [arXiv:2205.05358](https://arxiv.org/abs/2205.05358) [nucl-th]
65. S. Ryu, J.-F. Paquet, C. Shen, G. Denicol, B. Schenke, S. Jeon, C. Gale, *Phys. Rev. C* **97**, 034910 (2018). <https://doi.org/10.1103/PhysRevC.97.034910>. [arXiv:1704.04216](https://arxiv.org/abs/1704.04216) [nucl-th]
66. B. Schenke, C. Shen, P. Tribedy, *Phys. Rev. C* **99**, 044908 (2019). <https://doi.org/10.1103/PhysRevC.99.044908>. [arXiv:1901.04378](https://arxiv.org/abs/1901.04378) [nucl-th]
67. I. Karpenko, F. Becattini, *Nucl. Phys. A* **982**, 519 (2019). <https://doi.org/10.1016/j.nuclphysa.2018.10.067>. [arXiv:1811.00322](https://arxiv.org/abs/1811.00322) [nucl-th]